



In-situ synthesis of magnetite/expanded graphite composite material as high rate negative electrode for rechargeable lithium batteries

Weidong Zhang^a, Wang Wan^a, Henghui Zhou^{a,*}, Jitao Chen^b, Xiaoya Wang^b, Xinxiang Zhang^a

^a College of Chemistry and Molecular Engineering, Peking University, Chengfu Road 202, Haidian District, Beijing 100871, China

^b Pulead Technology Industry Co., LTD., Changping Science Park, Beijing 102200, China

HIGHLIGHTS

- ▶ The key trick is the in-situ oxidation of ferrocene–EG π – π intercalation composite.
- ▶ Fe_3O_4 particles are well dispersed in EG layers with strong interaction.
- ▶ Detailed investigation on the Fe_3O_4 /EG composite material.
- ▶ Unique hierarchical structure results in excellent cell performances.

ARTICLE INFO

Article history:

Received 24 July 2012

Received in revised form

10 September 2012

Accepted 13 September 2012

Available online 20 September 2012

Keywords:

Lithium ion battery

Intercalation compound

Interaction

Magnetite

Expanded graphite

ABSTRACT

Magnetite (Fe_3O_4)/expanded graphite (EG) composite material is prepared through the oxidation progress of ferrocene–graphite intercalation compound in acetone solution. The reactions occur in this system and lead to in-situ synthesis of the composite with nanosized magnetite and expanded graphite. Due to the lithium insertion/extraction experiment, the Fe_3O_4 /EG composite material shows high reversible capacities (ca. 720 mA h g^{-1} at 120 mA g^{-1} charge current) and excellent rate performances (ca. 630 mA h g^{-1} at 600 mA g^{-1} , 420 mA h g^{-1} at 6000 mA g^{-1} and 360 mA h g^{-1} at 9000 mA g^{-1} charge current). Owing to the strong interaction between Fe_3O_4 and EG from in-situ synthesis, it is demonstrated that these properties of this novel Fe_3O_4 /EG composite material will be an idea candidate for the negative electrode material of high-current lithium ion battery.

© 2012 Elsevier B.V. All rights reserved.

1. Introduction

With the increasing demand of high energy and power density [1–4], in the last two decades, lithium ion battery negative electrode materials based on transition metal oxides (M_xO_y , $\text{M} = \text{Fe}, \text{Co}, \text{Ni}, \text{Cu}$, etc.) have attracted considerable attention because of their high specific capacities [5–8]. For example, the theory specified capacity of Fe_3O_4 is 928 mA h g^{-1} , much higher than 372 mA h g^{-1} of the commercial graphite negative electrode material. Moreover, these materials composed of Fe_3O_4 are of environmental friendliness and natural abundance. While owing to the large volume change during battery charge and discharge progresses, the structure of Fe_3O_4 usually collapses. Thus these negative electrode materials disintegrate resulting in capacity fade and poor life

performance. To deal with this drawback in the electrode materials based on Fe_3O_4 , many approaches have been employed, such as carbon coating [5,8–12], nanostructure [13–15], modified by electronically conductive phases and decreasing the size of particles [16–18]. And these methods make Fe_3O_4 or its composites more suitable for high energy-density lithium ion battery. However, these high specific capacity materials are still suffering from the rapid capacity fading and bad rate performance because of Fe_3O_4 particle pulverization.

On the other hand, being a kind of naturally abundant and low cost material, graphite and its derivatives [19,20] are widely used in our modern lives and scientific research. Expanded graphite (EG), as the most important graphite derivative, is commonly obtained via thermal treatment of graphite intercalation compound. It is well known that EG is much lighter with a rather high specific surface and contains abundant pores ranging from 2 nm to $10 \mu\text{m}$ [21,22], maintaining layered structure similar to natural graphite flake. Recently, researchers have developed composite materials based on

* Corresponding author. Tel./fax: +86 10 62757908.

E-mail address: hzhzhou@pku.edu.cn (H. Zhou).

expanded graphite, such as tetrabutylammonium–EG [23], PPy–EG [24], TiO_2 –EG [25], and et al. [26,27]. While to the best of our knowledge, there is few report on the synthesis of Fe_3O_4 /EG composite materials with good interfacial interaction for lithium ion battery. This is because Fe_3O_4 is typically synthesized in the solution, not feasible to fabricate the composite material that Fe_3O_4 is well dispersed or embedded in the EG layers.

So herein, for the first time, we report in-situ synthesis of Fe_3O_4 /EG composite material with excellent rate and cycle performances as superior negative electrode material for lithium ion battery. The process is carried out as following: 1) driven by the π – π conjugate interaction [28,29], ferrocene is stable and enriched up in expanded graphite using acetone as the solvent; 2) via the oxidation of ferrocene–EG intercalation composite and follow-up heat treatment, Fe_3O_4 /EG composite material is obtained. The unique composites can 1) keep the structural stability in case of Fe_3O_4 particles uniform dispersion in EG layers; 2) provide appropriate buffer space to accommodate the volume change during the electrochemical investigation; 3) exhibit excellent conductivity performance by using EG as the matrix material; and 4) show wonderful electrochemical properties during rate and cycle cell tests because of the strong interaction between Fe_3O_4 particles and EG layers. It is found that the Fe_3O_4 /EG composite materials have the advantages of the active material Fe_3O_4 and the matrix material EG, and show a large reversible capacity, excellent cycle stability, and enhanced rate performance.

2. Experimental section

2.1. Synthesis of negative electrode material

Fe_3O_4 /EG composite material was fabricated by an in-situ synthesis method as following: The starting materials were ferrocene (98% Sinopharm Chemical Reagent Co., Ltd), hydrogen peroxide (H_2O_2 30% G.R. Beijing Chemical Works), expanded graphite (EG Qingdao Graphite Material Co., Ltd), acetone (Beijing Chemical Works) and ethylene glycol (Beijing Chemical Works).

In a typical synthesis, ferrocene (12.055 g) was dissolved in acetone (300 mL) to form a clear solution at 100 °C for 2 h. EG (1.0 g) was added into above solution with vigorous stirring for 8 h. When the temperature cooled down to 50 °C, H_2O_2 (11.104 g) was added into the above solution. Then the solution was maintained at 100 °C for 12 h and allowed to cool down to room temperature naturally. The gray precipitate was washed by acetone/ethanol for several times and vacuum-dried at 50 °C for 8 h. In order to get Fe_3O_4 /EG composite material, the gray precipitate was calcined under nitrogen atmosphere in two consecutive steps: at 50 °C for 0.5 h and 550 °C for 1.0 h.

2.2. Characterization of synthesized materials

The morphologies of the as-prepared Fe_3O_4 /EG composite material and EG were characterized by scanning electron microscope (SEM, Hitachi-530) and transmission electron microscope (TEM, JEOL JEM-2010). N_2 adsorption/desorption isotherms were

carried out using a Micromeritics ASAP 2010 (USA) analyzer at liquid nitrogen temperature.

Crystal structure of the Fe_3O_4 /EG composite material was characterized by X-ray scattering (XRD) carried out on Bruker D8 Advance X-ray diffractometer with Cu K α radiation ($\lambda = 1.5405 \text{ \AA}$).

And TGA data of the Fe_3O_4 /EG composite material was obtained by thermal analyzer TGA/DSC 1 from Mettler Toledo. X-ray photoelectron energy spectra data (XPS) were recorded using monochromatic Al K α X-ray sources with 30 eV pass energy in 0.5 eV step over an area of $650 \mu\text{m} \times 650 \mu\text{m}$ to the sample (degassed under a high vacuum condition to remove the adsorbed water and oxygen). Brunauer–Emmett–Teller test were measured with an ASAP 2020 Micromeritics Instrument at 77 K.

2.3. Electrochemical evaluation

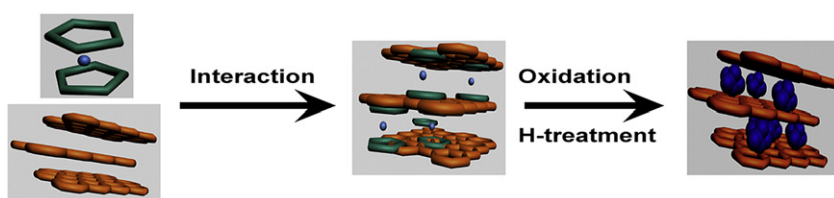
To prepare the negative electrode, polyvinylidene difluoride (PVDF, Alfa) was dissolved in N-methylpyrrolidinone (NMP), and then Fe_3O_4 /EG and super-P carbon black (Alfa) were added (Fe_3O_4 /EG, super-P and PVDF were mixed in 80:10:10 by weight) and the solution changed into slurry. The slurry was cast on the copper foil and dried at 120 °C under vacuum for 8 h. Then the film was pressed at a pressure of about 10 MPa and punched into round disks with 12 mm in diameter for further experiments. The electrode active thickness was 11 μm and active mass was about 3.0 mg.

Standard 2032 coin cell was assembled in a dry Ar-filled glove box to test the electrochemical properties of the Fe_3O_4 –EG material. Lithium metal foil was used as the counter electrode and 1 M LiPF_6 in EC/EMC/DEC (1:1:1 by vol.) as the liquid electrolyte. A Celgard 2400 microporous polypropylene membrane was used as the separator. After aging for 4 h, the cell was charged and discharged in the voltage range between 0.005 V and 3.0 V at a current density of 1 C (600 mA g^{-1} was assumed to be the 1 C rate current) and 5 C for 100 cycles. The rate capability was measured by discharging at 0.2 C current and then charging at different current densities: 0.2 C, 1 C, 2 C, 5 C, 10 C, 15 C and 0.2 C.

3. Results and discussion

In this system, acetone served as the solvent, ferrocene as the iron source, expanded graphite as the matrix material, and H_2O_2 as the oxidant respectively. The Fe_3O_4 /EG composite material was fabricated with an in-situ oxidation of ferrocene–EG composite and follow-up heat treatment. As seen in Scheme 1, the procedure of Fe_3O_4 /EG composite material involves 3 steps: ferrocene is enriched up in expanded graphite forming ferrocene–EG intercalation composite; ferrocene–EG intercalation composite is oxidized when the oxidant H_2O_2 is added into the solution; then the precipitate is heat-treated under 550 °C for 1 h and changed into Fe_3O_4 /EG composite material. The obtained Fe_3O_4 /EG composite material allows perfect Fe_3O_4 particle protection and wonderful overall ion and electron conductivity.

Morphology of the Fe_3O_4 /EG composite material is shown in Fig. 1 by scanning electron microscope (SEM). For the first case as



Scheme 1. Synthesis of Fe_3O_4 /EG composite material.

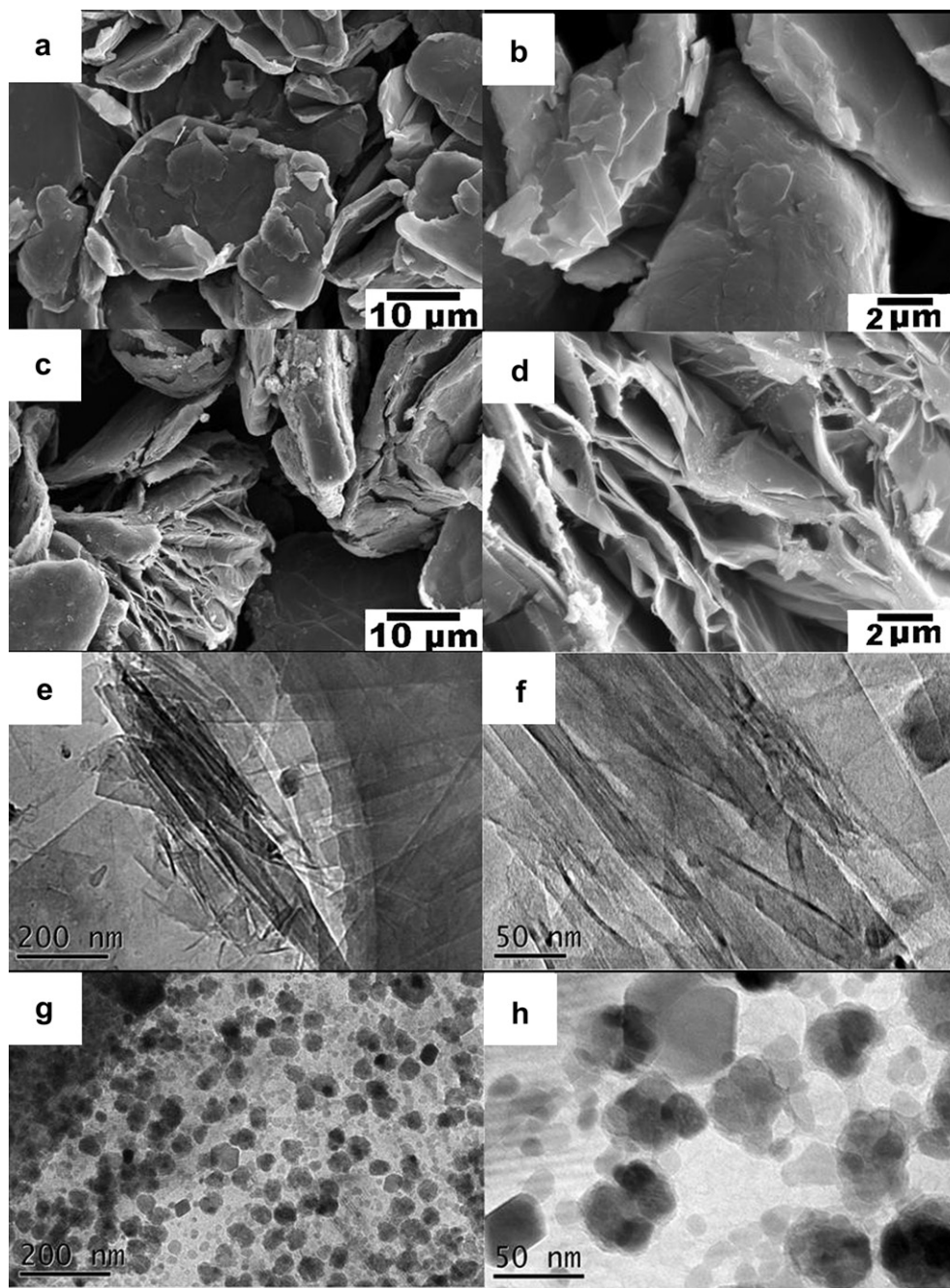


Fig. 1. SEM images of EG (a, b) and Fe₃O₄/EG composite material (c, d), and TEM images of EG (e, f) and Fe₃O₄/EG composite material (g, h).

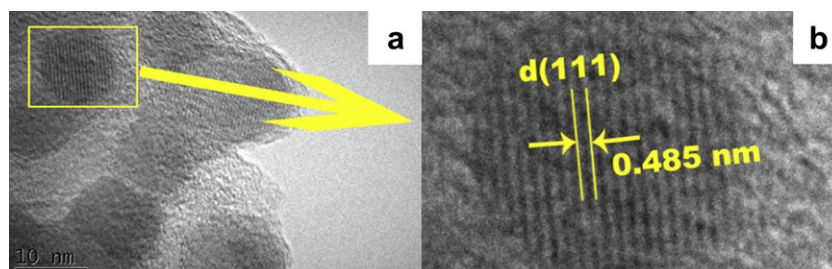


Fig. 2. High-resolution TEM images of Fe₃O₄/EG composite material.

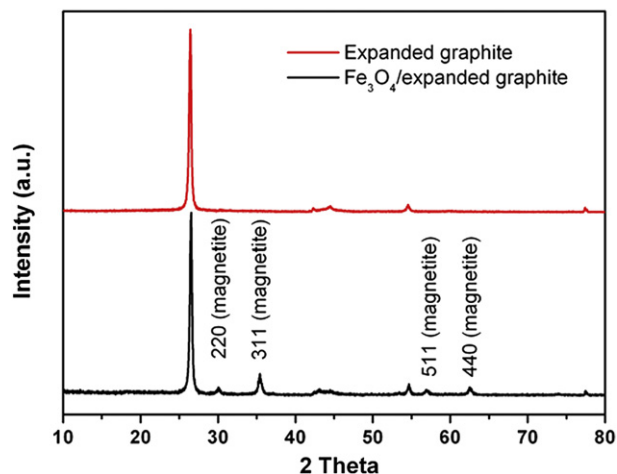


Fig. 3. XRD patterns of EG and as-obtained $\text{Fe}_3\text{O}_4/\text{EG}$ composite material.

shown in Fig. 1a, the raw material EG shows a layered aggregative structure with some separated graphite layers nearby. Fig. 1b is a magnificent picture of the raw materials EG, and it can be seen that EG surface is quite smooth. While compared to the raw material, the graphite layer in $\text{Fe}_3\text{O}_4/\text{EG}$ composite material opens its blades, and there are obvious spaces appeared as shown in Fig. 1c. And there is few isolated Fe_3O_4 particle out of EG in the composite. From the enlarged picture in Fig. 1d, it is noted that the graphite layers of $\text{Fe}_3\text{O}_4/\text{EG}$ composite materials are rather rough with uniform particles attached onto the graphite layers. These particles are in-situ created during the oxidation and subsequent heat treatment process. In order to investigate the microstructure of the representative samples of Fig. 1a and c in more detail, transmission electron microscope (TEM) test is carried out. It can be seen from Fig. 1e and f (enlarged image) that the raw material EG shows a layer-like morphology, and there is no inorganic particle between the graphite layers. While as to the composite material, there are lots of Fe_3O_4 particles with uniform size and well dispersion coating on the graphite layers. As seen in Fig. 1g, the average diameter of the Fe_3O_4 particles is 25 nm. In addition, it is clearly seen from the enlarged image Fig. 1h that a Fe_3O_4 particle is half-covered by a single graphite layer. This scene shows the evidence that most of the Fe_3O_4 particles are in-situ synthesized

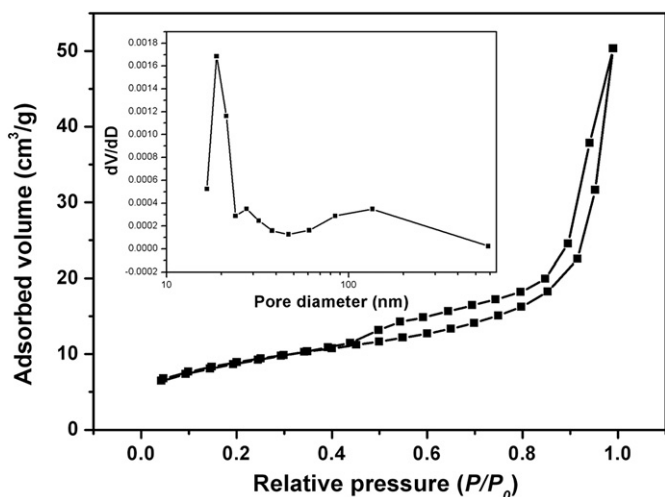


Fig. 4. Nitrogen adsorption–desorption isotherms at 77 K with corresponding BJH desorption pore size distributions (inset).

and embedded in the EG graphite layers. The HRTEM image (Fig. 2a) taken on an edge of $\text{Fe}_3\text{O}_4/\text{EG}$ composite material shows that the Fe_3O_4 particles embedded in the graphite layers are well crystallized with the diameter of about 25 nm. Fig. 2b displays crystal planes with a d-spacing of 0.485 nm, corresponding to the (111) plane of Fe_3O_4 . And according to TGA-DSC test (seen in Figure S1), the Fe_3O_4 content of $\text{Fe}_3\text{O}_4/\text{EG}$ composite material is 34.62 wt%.

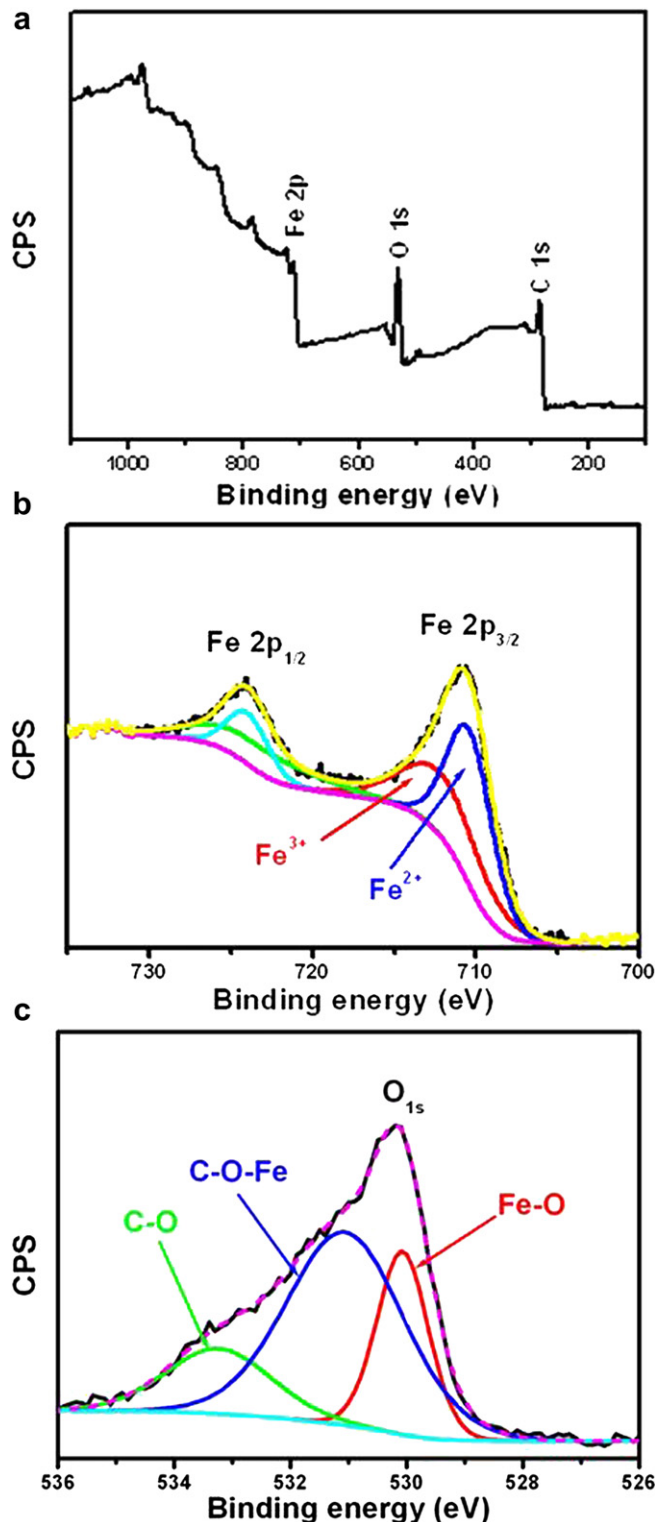


Fig. 5. XPS data of as-obtained $\text{Fe}_3\text{O}_4/\text{EG}$ composite material (a), the expanded spectra of $\text{Fe} 2p$ (b), and the expanded spectra of $\text{O} 1s$ (c).

In order to clarify the as-obtained material structure, X-ray diffraction (XRD) experiments are carried out as seen in Fig. 3. In the pattern of expanded graphite diffraction peaks are observed at $2\theta = 26.4, 42.2, 44.4, 54.5$ and 77.2° : these peaks can be indexed to the Graphite-2H (002), (100), (101), (004) and (110) faces, respectively (Joint Committee on Powder-Diffraction Standards (JCPDS) PDF No. 41-1487), which is representative of expanded graphite in the crystalline phase. And in the pattern of $\text{Fe}_3\text{O}_4/\text{EG}$ composite material, besides those peaks corresponding to expanded graphite, peaks at $2\theta = 30.1, 35.5, 57.0$ and 62.6° can be assigned to the cubic magnetite (220), (311), (511) and (440) faces respectively with cell constant $a = 0.8391$ nm (JCPDS PDF No. 65-3107). That is to say that the XRD patterns conform the formation of $\text{Fe}_3\text{O}_4/\text{EG}$ composite material, and there are no diffraction peaks for impurities, implying the controllable process in this reaction system.

In Fig. 4, it is shown the nitrogen adsorption–desorption isotherm and the corresponding Barrett–Joyner–Halenda (BJH) desorption pore size distribution of the as-prepared $\text{Fe}_3\text{O}_4/\text{EG}$ composite material. For the relative pressure P/P_0 ranging from 0.5 to 0.9, the isotherm feature hysteresis has a well-defined step between desorption and adsorption branches, indicating the sample as a characteristic mesoporous material [30]. According to the BJH analysis (inset), there are two pore size distribution peaks for $\text{Fe}_3\text{O}_4/\text{EG}$ composite material: one sharp peak is in the range 20 nm, responding to the pores forming by Fe_3O_4 particles; another broad peak is in the range 160 nm, responding to the expanded graphite layers. These pore spaces are helpful to buffer the volume expansion during Li insertion [9,31]. And BET surface area of the $\text{Fe}_3\text{O}_4/\text{EG}$ composite material is $30.70 \text{ m}^2 \text{ g}^{-1}$, rather higher than that of raw material expanded material ($12.48 \text{ m}^2 \text{ g}^{-1}$). This sandwich-like microstructure as Fe_3O_4 particles embedded in graphite layers of the sample facilitates larger area for the electrolyte contact, resulting in fast Li ion mobility and lower charge-transfer resistance, in return reducing the local density for a given current [32].

As a powerful tool for electronic and structural investigations [33,34], X-ray photoelectron spectroscopy (XPS) pattern of the $\text{Fe}_3\text{O}_4/\text{EG}$ composite material is recorded to get more banding information, which reveals the strong interaction between Fe_3O_4 particles and EG matrix in the obtained composite material (see Fig. 5). As shown in Fig. 5a, there are Fe, C and O elements in the sample related to Fe_3O_4 and EG. After a Shirley background correlation, the curves of Fe and O are carried out by using Gaussian–Lorentzian peak shape. In Fig. 5b, binding energies of $\text{Fe} 2p$ at 711.5 eV and 725.4 eV, which are the characteristic doublets of $\text{Fe} 2p_{3/2}$ and $2p_{1/2}$ core-level spectra of ferric oxides, are observed in the $\text{Fe}_3\text{O}_4/\text{EG}$ composite material that is consistent with the oxidation state of Fe in Fe_3O_4 [35,36]. Moreover, as shown in Fig. 5c,

the binding energies of O1s fitted to 533.3 eV, 531.2 and 530.0 eV, which are assigned as C–O bond from the original oxygen in EG, C–O–Fe bond from the interaction between Fe_3O_4 particle and EG matrix [37], and Fe–O bond from Fe_3O_4 particle [36,38] respectively, are also observed. The existing of C–O–Fe bond indicates that there exists a rather strong interaction between Fe_3O_4 particle and EG matrix in the product, provides a stable structure and should result in excellent electrochemical performance.

3.1. Electrochemical performance

In order to well understand the specific capacity, cyclic stability and rate performance of the $\text{Fe}_3\text{O}_4/\text{EG}$ composite materials in lithium ion battery, the electrochemical properties with respect to Li insertion/extraction are investigated. The experiments are carried out by using galvanostatic cycling at room temperature in coin cells with metallic lithium as the negative electrode.

The charge capacity of only EG is $293.5 \text{ mA h g}^{-1}$ (provided in Figure 2s) at discharge/charge current density of 74 mA g^{-1} . The first-five discharge/charge curves (seen in Figure 3s) of the $\text{Fe}_3\text{O}_4/\text{EG}$ composite material are investigated with a potential plateau at about 0.7 V versus Li^+/Li , which are close to that reported in the literature [39]. During the first-five cycles, $\text{Fe}_3\text{O}_4/\text{EG}$ composite materials show rather high specific charge capacity about 680 mA h g^{-1} , and there is some increasing in specific capacity obviously from cycle 2 to cycle 5 (743 mA h g^{-1}).

Fig. 6a shows the rate performances of $\text{Fe}_3\text{O}_4/\text{EG}$ composite material. During the experiments, the samples are discharged/charged at different C-rates. For each charge rate of 0.2 C (0.12 A g^{-1}), 1 C (0.6 A g^{-1}), 2 C (1.2 A g^{-1}), 5 C (3 A g^{-1}), 10 C (6.0 A g^{-1}), and 15 C (9 A g^{-1}), the charge capacities and capacity retains (as seen in Fig. 6b) are obtained as $679.2 \text{ mA h g}^{-1}$ (setting as 100% retain), $638.7 \text{ mA h g}^{-1}$ (94.04% retain), $628.6 \text{ mA h g}^{-1}$ (92.55% retain), 539 mA h g^{-1} (79.36% retain), $418.7 \text{ mA h g}^{-1}$ (61.65% retain) and $360.6 \text{ mA h g}^{-1}$ (53.09% retain), respectively. When the current rate is again reduced back to 0.2 C, the capacity just shows a low initial capacity $700.2 \text{ mA h g}^{-1}$, then increases to $721.1 \text{ mA h g}^{-1}$ gradually. This rate performance is excellent ($418.7 \text{ mA h g}^{-1}$ under 6.0 A g^{-1} and $360.6 \text{ mA h g}^{-1}$ under 9.0 A g^{-1}), and there are no similar results reported in other literature. As shown in Fig. 7, the cycling performances of $\text{Fe}_3\text{O}_4/\text{EG}$ composite materials are evaluated between 0.005 and 3.0 V vs. Li^+/Li at the discharge/charge rates of 1 C (0.6 A g^{-1}) and 5 C (3 A g^{-1}) and the reversible capacities are 615 mA h g^{-1} and 526 mA h g^{-1} respectively. After 100 cycles, the cells show exceptional stability without capacity fade. When the current density was lowered to 120 mA g^{-1} , the capacities completely recovered to those pristine cells after such giant current

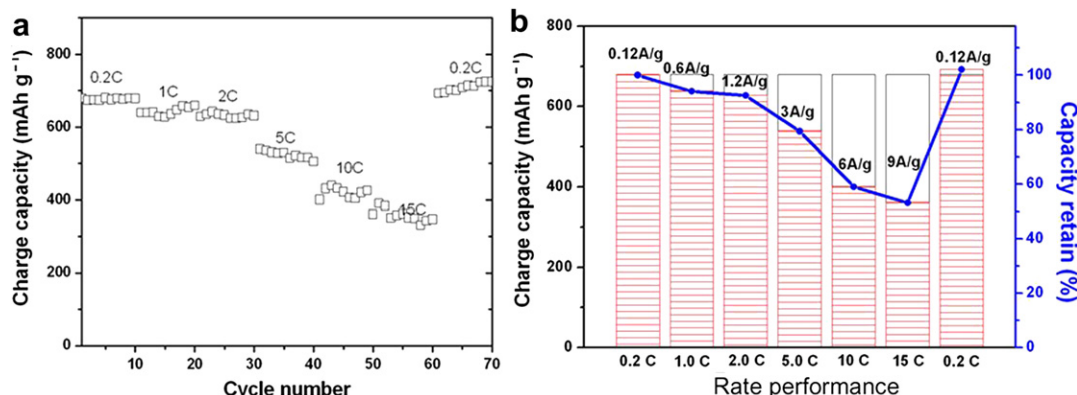


Fig. 6. Rate performances (a) and capacity retains (b) of as-obtained $\text{Fe}_3\text{O}_4/\text{EG}$ composite material in the voltage range 0.005–3.0 V at different current rates.

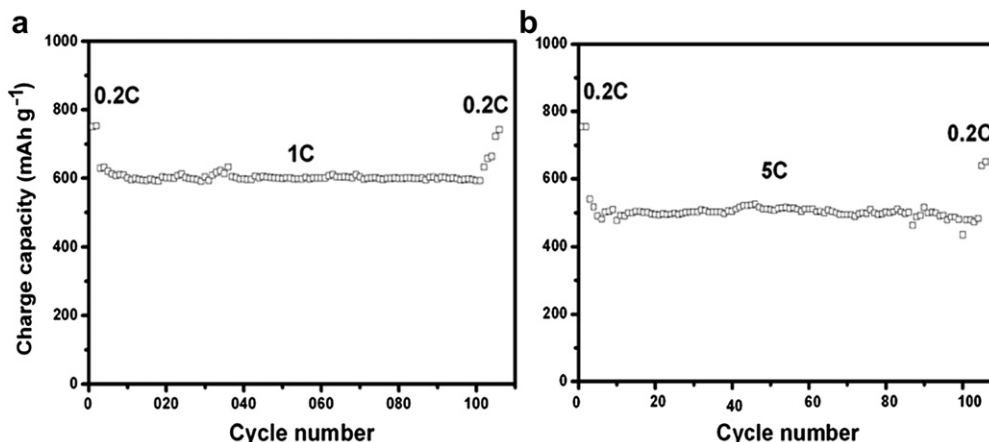


Fig. 7. Cycle performances of as-obtained $\text{Fe}_3\text{O}_4/\text{EG}$ composite material in the voltage range 0.005–3.0 V at 1 C (a) and 5 C (b).

densities. These results clearly show that the unique sandwich-like morphology by means of in-situ oxidation of ferrocene–EG π – π intercalation composite as in $\text{Fe}_3\text{O}_4/\text{EG}$ composite material, plays an important role in improving the rate capability. The EG matrix not only improves the local conductivity but also prevents the detachment and aggregation of possibly pulverized Fe_3O_4 nanoparticles during cycling. And the unique morphology is helpful to reduce current density and provide proper buffer space. Based on these factors mentioned above, the properties of $\text{Fe}_3\text{O}_4/\text{EG}$ composite material as lithium ion battery negative electrode material are greatly enhanced.

4. Conclusions

In summary, we report an in-situ method to fabricate $\text{Fe}_3\text{O}_4/\text{EG}$ composite material through the oxidation of ferrocene–EG π – π intercalation composite used as lithium ion battery negative electrode. The as-obtained sample has the sandwich-like hierarchical morphology, using EG as the matrix and Fe_3O_4 nanoparticles the stuffing. Due to the unique nano/micro-hierarchical structure, electric matrix and space buffer effect, the $\text{Fe}_3\text{O}_4/\text{EG}$ composite material exhibits high capacity, good cycle stability and enhanced rate capability. And in-situ synthesis by the advantage of π – π conjugation is a promising method to enhance the performance of transition metal oxides as lithium ion battery negative electrode materials.

Acknowledgements

The authors appreciate the financial support of the National Basic Research Program of China (No. 2009CB220100), the National High Technology Research and Development Program of China (No. 2009AA035200) and A* Star Singapore–China Joint Research Programme (No. 2012DFG52130).

Appendix A. Supplementary data

Supplementary data related to this article can be found at <http://dx.doi.org/10.1016/j.jpowsour.2012.09.033>.

References

- [1] A.S. Arico, P. Bruce, B. Scrosati, J.-M. Tarascon, W. van Schalkwijk, *Nat. Mater.* 4 (2005) 366–377.
- [2] K. Kang, *Science* 311 (2006) 977–980.
- [3] M. Armand, J.M. Tarascon, *Nature* 451 (2008) 652–657.

- [4] X. Ji, K.T. Lee, L.F. Nazar, *Nat. Mater.* 8 (2009) 500–506.
- [5] W.-M. Zhang, X.-L. Wu, J.-S. Hu, Y.-G. Guo, L.-J. Wan, *Adv. Funct. Mater.* 18 (2008) 3941–3946.
- [6] W. Chen, S. Li, C. Chen, L. Yan, *Adv. Mater.* 23 (2011) 5679–5683.
- [7] H. Liu, G. Wang, J. Wang, D. Wexler, *Electrochem. Commun.* 10 (2008) 1879–1882.
- [8] L. Wang, Y. Yu, P.C. Chen, D.W. Zhang, C.H. Chen, *J. Power Sources* 183 (2008) 717–723.
- [9] Y. He, L. Huang, J.S. Cai, X.M. Zheng, S.G. Sun, *Electrochim. Acta* 55 (2010) 1140–1144.
- [10] S.L. Jin, H.G. Deng, D.H. Long, X.J. Liu, L.A. Zhan, X.Y. Liang, W.M. Qiao, L.C. Ling, *J. Power Sources* 196 (2011) 3887–3893.
- [11] M.M. Rahman, J.Z. Wang, M.F. Hassan, Z.X. Chen, H.K. Liu, *J. Alloy Compd.* 509 (2011) 5408–5413.
- [12] J. Wang, X.M. Liu, H. Yang, X.D. Shen, *J. Alloy Compd.* 509 (2011) 712–718.
- [13] S.Q. Wang, J.Y. Zhang, C.H. Chen, *J. Power Sources* 195 (2010) 5379–5381.
- [14] L.Q. Chen, W.P. Liu, J.L. Chen, X.F. Yang, J. Liu, X.H. Fu, M.M. Wu, *Sci. China Chem.* 54 (2011) 923–929.
- [15] M. Nagao, M. Otani, H. Tomita, S. Kanzaki, A. Yamada, R. Kanno, *J. Power Sources* 196 (2011) 4741–4746.
- [16] J.P. Liu, Y.Y. Li, H.J. Fan, Z.H. Zhu, J. Jiang, R.M. Ding, Y.Y. Hu, X.T. Huang, *Chem. Mater.* 22 (2010) 212–217.
- [17] H.N. Duan, J. Gnanaraj, X.P. Chen, B.Q. Li, J.Y. Liang, *J. Power Sources* 185 (2008) 512–518.
- [18] M. Zhang, D. Lei, X. Yin, L. Chen, Q. Li, Y. Wang, T. Wang, *J. Mater. Chem.* 20 (2010) 5538.
- [19] C. Kim, K.S. Yang, M. Kojima, K. Yoshida, Y.J. Kim, Y.A. Kim, M. Endo, *Adv. Funct. Mater.* 16 (2006) 2393–2397.
- [20] E. Kang, Y.S. Jung, G.-H. Kim, J. Chun, U. Wiesner, A.C. Dillon, J.K. Kim, J. Lee, *Adv. Funct. Mater.* 21 (2011) 4349–4357.
- [21] Y.F. Zhao, M. Xiao, S.J. Wang, X.C. Ge, Y.Z. Meng, *Compos. Sci. Technol.* 67 (2007) 2528–2534.
- [22] W. Zheng, S.-C. Wong, *Compos. Sci. Technol.* 63 (2003) 225–235.
- [23] W. Sirisaksoontorn, A.A. Adenuga, V.T. Remcho, M.M. Lerner, *J. Am. Chem. Soc.* 133 (2011) 12436–12438.
- [24] S. Konwer, J. Maiti, S.K. Dolui, *Mater. Chem. Phys.* 128 (2011) 283–290.
- [25] Y. Yu, N. Zhao, C. Shi, C. He, E. Liu, J. Li, *Int. J. Hydrogen Energy* 37 (2012) 5762–5768.
- [26] X. Zhao, C.M. Hayner, M.C. Kung, H.H. Kung, *Adv. Energy Mater.* 1 (2011) 1079–1084.
- [27] K. Evanoff, A. Magasinski, J. Yang, G. Yushin, *Adv. Energy Mater.* 1 (2011) 495–498.
- [28] Y. Gao, D. Ma, G. Hu, P. Zhai, X. Bao, B. Zhu, B. Zhang, D.S. Su, *Angew. Chem. Int. Ed.* 50 (2011) 10236–10240.
- [29] Y. Gao, G. Hu, W. Zhang, D. Ma, X. Bao, *Dalton Trans.* 40 (2011) 4542.
- [30] D.H.E.K.S.W. Sing, R.A.W. Haul, L. Moscou, R.A. Pierotti, J. Rouquerol, T. Siemieniowska, *Appl. Chem.* 57 (1985).
- [31] P.C. Lian, X.F. Zhu, H.F. Xiang, Z. Li, W.S. Yang, H.H. Wang, *Electrochim. Acta* 56 (2010) 834–840.
- [32] C.W. Sun, S. Rajasekhara, J.B. Goodenough, F. Zhou, *J. Am. Chem. Soc.* 133 (2011) 2132–2135.
- [33] L. Tang, Y. Wang, Y. Li, H. Feng, J. Lu, J. Li, *Adv. Funct. Mater.* 19 (2009) 2782–2789.
- [34] A. Ghirri, V. Corradini, C. Cervetti, A. Candini, U. del Pennino, G. Timco, R.J. Pritchard, C.A. Muryn, R.E.P. Winpenny, M. Affronte, *Adv. Funct. Mater.* 20 (2010) 1552–1560.
- [35] X. Teng, D. Black, N.J. Watkins, Y. Gao, H. Yang, *Nano Lett.* 3 (2003) 261–264.
- [36] P.C.J. Graat, M.A.J. Somers, *Appl. Surf. Sci.* 100–101 (1996) 36–40.
- [37] J. Zhou, H. Song, L. Ma, X. Chen, *RSC Adv.* 1 (2011) 782.
- [38] C. Combéllas, M. Delamar, F. Kanoufi, J. Pinson, F.I. Podvorica, *Chem. Mater.* 17 (2005) 3968–3975.
- [39] I.A. Courtney, J.R. Dahn, *J. Electrochem. Soc.* 144 (1997) 2045–2052.